Structural effect of one-dimensional nanowire 2%Mn-5%Na$_2$WO$_4$/SiO$_2$ catalyst towards oxidative coupling of methane

I. Sereewatthanawut [a,b], V. Tongnan [c], R. Ampairojanawong [c], A. Makdee [c], N. Swadchaipong [c], P. Maneesard [c], M. Hartley [d], K. Li [e], U.W. Hartley [c,*]

[a] *King Prajadhipok's Institute, Bangkok 10210, Thailand*
[b] *Faculty of Engineering and Technology, Pathumthani University, Pathumthani 12000, Thailand.*
[c] *Chemical and Process Engineering, The Sirindhorn International Thai-German Graduate School of Engineering (TGGS), King Mongkut's University of Technology North Bangkok, Bangkok 10800, Thailand*
[d] *Chemical Engineering, Engineering Faculty, King Mongkut's University of Technology North Bangkok, Bangkok 10800, Thailand*
[e] *Chemical Engineering, Imperial College London, SW7 2AZ, UK*

ARTICLE INFO

ABSTRACT

Nanowire-structured 2%Mn-5%Na$_2$WO$_4$/SiO$_2$ was successfully synthesized and demonstrated superior catalytic performance compared to its powder form across the entire temperature range of 650–800 °C. In this study, the hydrothermal synthesis time for the nanowires was varied at 8, 12, 17, and 24 h, referred to as NWs-8, NWs-12, NWs-17, and NWs-24, respectively. NWs-12 exhibited the smallest diameter and the longest length among the synthesized nanowires. However, NWs-17 showed the best performance for the oxidative coupling of methane (OCM) process, despite having a relatively less impressive morphology. This superior performance could be attributed to the presence of Mn$_2$O$_3$ active species without interference from MnO$_2$, which was only observed in NWs-17 and NWs-24. The larger crystal size of NWs-24 contributed to its poorer performance compared to NWs-17. NWs-17 achieved a maximum C$_{2+}$ selectivity of 68% and a high CH$_4$ conversion rate of 21.8% under operating conditions of 775 °C, CH$_4$:O$_2$ = 4, and WHSV = 8572 ml/h/g.

1. Introduction

Methane (CH$_4$) is a greenhouse gas that is approximately 21 times more potent than CO$_2$, and therefore contributes significantly to global warming [1,2], if released at the same amount. As a result, effective management and control of methane utilization is crucial to slowing down the effects of global warming. Methane is considered an environmentally friendly fossil fuel. It is commonly found in natural gas and shale gas sources in large quantities throughout the world, which makes it widely available and affordable [3,4]. Researchers have been exploring ways to convert methane into high-value chemicals, precursors, or other fuels to maximize its potential benefits while reducing its impact on the environment. Methane is being increasingly used as an alternative energy source in many countries, for applications such as electricity generation, transportation, and industrial production. This is because methane provides the highest energy release of 891 kJ/mol [5] and produces relatively less carbon dioxide (CO$_2$) during combustion [5] compared to other hydrocarbon compounds.

Indirect methane conversion refers to the oxidation of methane to syngas (a mixture of CO and H$_2$) as an intermediate substance to convert to fuel and other chemicals, such as steam reforming (SRM) [6,7], dry reforming (DRM) [8–10] and partial oxidation of methane (POM) [11–13]. However, these indirect methane conversions generally require high operation cost which can be seen as a major limitation of such processes. On the other hand, direct methane conversions; i.e. methane pyrolysis or oxidative coupling of methane; advantage can directly convert methane into fuel which consist of pyrolysis [14,15] and oxidative coupling of methane (OCM) [16–18]. Methane (CH$_4$) is a stable tetrahedral molecule, requiring relatively high temperature and/or pressure to be broken down/converted to other valuables. This often results in unwanted reactions, undesired products, and therefore low selectivity. This challenge also applies to OCM (normally occurs at temperature range of 750 to 950 °C) where methane is converted to desired hydrocarbon compounds such as ethane (C$_2$H$_6$) and ethylene (C$_2$H$_4$) as shown in reactions (1) and (2). The product mixtures can be considered as C$_{2+}$.

$$2CH_4 + 0.5O_2 \rightarrow C_2H_6 + H_2O \; \Delta H^{\circ}_{298K} = -177 \; kJ/mol \quad (1)$$

$$2CH_4 + O_2 \rightarrow C_2H_4 + 2H_2O \; \Delta H^{\circ}_{298K} = -144 \; kJ/mol \quad (2)$$
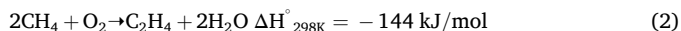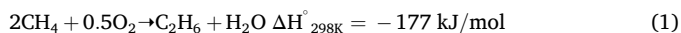
At such high temperatures, the C_{2+} product becomes more active than methane, resulting in the formation of CO_x (CO and CO_2) as an undesirable byproduct as reactions (3) and (4) which lowers not only methane conversion but also selectivity. Moreover, the CO_x formation during the high operating temperature is responsible for high methane conversion but low C_{2+} selectivity as reactions (5) and (6) which are called complete combustion and partial oxidation side reactions, respectively. Therefore, the oxygen concentration must be limited because high oxygen concentration would induce side reactions leading to CO_x products formation. Although at high temperatures are required to promote reactions (1) and (2), they can contribute to the oxidation of CH_4 and that of C_{2+} to produce CO_x causing a limitation of C_{2+} selectivity.

$$C_2H_6 + 2.5O_2 \rightarrow 2CO + 3H_2O \; \Delta H^{\circ}_{298K} = -757 \; kJ/mol \quad (3)$$

$$C_2H_4 + 2O_2 \rightarrow 2CO + 2H_2O \; \Delta H^{\circ}_{298K} = -752 \; kJ/mol \quad (4)$$

$$CH_4 + 2O_2 \rightarrow CO_2 + 2H_2O \; \Delta H^{\circ}_{298K} = -802 \; kJ/mol \quad (5)$$

$$CH_4 + 1.5O_2 \rightarrow CO + 2H_2O \; \Delta H^{\circ}_{298K} = -519 \; kJ/mol \quad (6)$$
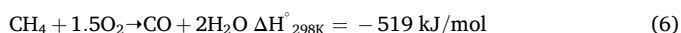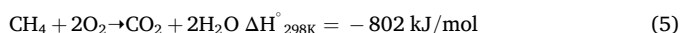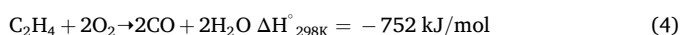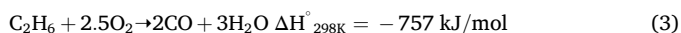
Furthermore, it is generally recognized that the acid-base properties of the catalysts, especially the concentration of basic sites on the surface, play a crucial role in the formation of C_{2+} hydrocarbons in the OCM reaction. The interpretation of the catalytic performance in terms of acid-base theory will contribute to the understanding of the reaction mechanism and thus enable the investigation of effective ways to improve the catalytic performance. F. Papa et al. [19] showed that methane is converted to products on two types of active sites via independent pathways: (i) the catalytic activity for C_{2+} formation is directly related to the overall basicity of catalysts (number of basic sites), and (ii) methane is oxidized to CO_2 (methane combustion) on acid sites. As a result, a strategy for increasing the performance of OCM catalysts must include the identification of molecules with optimal basic and acidic sites responsible for methane conversion.

As mentioned above, it is an essential consideration for improving overall process efficiency both in terms of catalyst properties and reaction conditions. An appropriate choice of catalyst can be chosen to maximize the process's performance. Many types of primary/binary metal and/or metal oxide supports such as Li/MgO [20,21], La$_2$O$_3$/CaO [22,23], Sr/La$_2$O$_3$ [24], BaSrTiO$_3$ [25], have been applied in the OCM process. Among these catalyst systems, Mn-Na$_2$WO$_4$/SiO$_2$ [26–28] had been reported to give the best catalytic performance, providing 20–30% of methane conversion, 60–80% of C_{2+} selectivity, relatively good stability depending on the preparation method.

Our approach to increase the process performance is to develop the catalyst with suitable properties that is active at low OCM reaction temperature to minimize the unwanted side reactions and achieve high C_{2+} selectivity. The catalyst design plays an important part because it can reduce the required activation energy for the C_{2+} production reaction and enhance its rate. The activation energy of the reaction is related to the accessibility of the reactant to the catalyst's active sites, depending on the shape, size, and morphology of the catalyst. These factors can be designed by many choices of synthesis method, type of precursor or preparation conditions. Nano-structured catalyst with various shapes (i. e., La$_2$O$_3$ nanorod [29], La$_2$O$_3$ nanosheets [30], Sr-La$_2$O$_3$ nanofiber [31], La$_2$O$_3$-CeO$_2$ nanofiber [32–34], and Mn-doped TiO$_2$ nanofiber [35]) have been reported to be able to lower the OCM operating temperature down by 20–21% (from the range of 750–950 °C to 500–750 °C).

This work therefore focuses on developing the most promising nanowire-structured Mn-Na$_2$WO$_4$/SiO$_2$. The catalytic performances of the synthesized catalysts were tested in a packed-bed reactor for OCM

reaction by varying the reaction temperature. The catalyst properties such as phase structure, shape/morphology and acidity/basicity were characterized by XRD, FE-SEM, CO_2-TPD and NH_3-TPD. In this study, we compared the powder form of Mn-Na$_2$WO$_4$/SiO$_2$ with its nano-structured form, which was prepared at different hydrothermal time (8–24 h).

2. Experiment

2.1. Preparation of 2%Mn-5%Na$_2$WO$_4$/SiO$_2$

0.032 mol of Manganese sulphate (MnSO$_4$.H$_2$O, KEMAUS, 98% purity), 0.08 mol of ammonium sulphate ((NH$_4$)$_2$SO$_4$, KEMAUS, 99% purity), and 0.032 mol of ammonium persulphate ((NH$_4$)$_2$S$_2$O$_8$, KEMAUS, 98% purity) were each dissolved in 40 ml of DI water separately. The three solutions were mixed and adjusted to 160 ml of the total volume by DI water. The mixed solution was transferred to 200 ml Teflon-lined autoclave and heated at 140 °C for 8, 12, 17, and 24 h, where the resulting catalysts would be referred to as NWs-8, NWs-12, NWs-17 and NWs-24, respectively. MnO$_2$ nanowires were afterward filtrated, washed by DI water, and dried in the oven at 100 °C overnight. On the other hand, the powdered 2%Mn-5%Na$_2$WO$_4$-SiO$_2$ was prepared by incipient wetness impregnation (IWI) technique, to compare with the MnO$_2$ nanowires. The corresponding amount of MnO$_2$ nanowires, sodium tungsten (Na$_2$WO$_4$.2H$_2$O, sigma aldrich, 99% purity), and fumed silica commercial (SiO$_2$, Ajax finechem, 98% purity) were stoichiometrically calculated and mixed with 100 ml of DI water. The mixed solution was heated to 90 °C until it was thickened. The resulting catalysts were dried at 100 °C overnight, calcined at 400 °C for 6 h, and sieved to 75–180 μm.

2.2. Characterizations

The morphology of all the nanowire MnO$_2$ without calcination was characterized using field emission scanning electron microscope (FE-SEM, SU8030) with an accelerating voltage of 3 to 5 kV and magnification of 100,000× while the morphology and EDS spectra of NWs-12 before (150,000×) and after (15,000×) OCM reaction were investigated using Thermo Scientific Phenom Pharos G2 Desktop Field Emission Gun-Scanning Electron Microscope (FEG-SEM) with an accelerating voltage of 15 kV. The phase structure of the synthesized nanowires was characterized using X-ray diffraction (XRD, Rigaku SmartLab SE system) using Cu K$_{\alpha}$ radiation ($\lambda = 1.5410$ Å) at an accelerating voltage of 40 kV, current of 100 mA, and a D/teX Ultra 250 detector. The scanning range of 2θ was set from 10° to 80° with a step width of 0.010 and scanning speed of 5°/min. The acid and basic sites of the catalyst's surface were characterized using NH_3 and CO_2 temperature-programmed desorption (TPD), respectively. Before each of the TPD processes, the catalyst sample (0.7 g) was pretreated at 150 °C for 1 h with a flow rate of 100 ml/min of Argon gas (Ar), before being cooled down to room temperature (25 °C). After pretreatment, the catalyst sample was exposed to the corresponding gas mixtures at different temperatures. Individually, 50 ml/min of 5%vol. NH_3/Ar was fed at 50 °C or 100 ml/min of 5%vol. CO_2/Ar was fed at 100 °C for 2 h to the system in which it was cooled down to room temperature by continuing the gas flow and left overnight. During the TPD process, the temperature of the packed-bed reactor was increased from room temperature to 950 °C with a heating rate of 5 °C/min under a flow rate of 100 ml/min for Ar. The gas desorption profiles (NH_3 or CO_2) were measured in real-time by a mass spectrometer (GSD 320, OmniStar).

2.3. Activity study for OCM

The catalytic performances of 2%Mn-5%Na$_2$WO$_4$-SiO$_2$ catalysts were tested for the OCM reaction using a packed-bed reactor. The reactor consisted of a quartz tube with an inner diameter of 9 mm and a

length of 25 cm as shown in Fig. 1. The synthesized catalyst (0.7 g) was packed in a quartz tube along with a quartz wool support and placed in a tubular furnace with a 20 cm heating zone, coupled with temperature controller system. Any of the interest catalyst was pre-treated at 650 °C for 1 h under a flow rate of 100 ml/min of Ar, prior to the start of the OCM reaction. This pretreatment was done to activate the catalysts by removing any impurities or unwanted species present on the catalyst surface (surface area clearance), and to maximize the catalytic performance of the synthesized catalysts to their best possible. The reactants; 16 ml/min of CH_4, 10 ml/min of 40% O_2/Ar (molar ratio of CH_4:O_2 = 4, WHSV = 8572 ml/h/g); were co-fed with a total flow rate to 100 ml/min using Ar as a make-up gas. The operation temperature was varied at 650, 675, 700, 725, 750, 775, and 800 °C. After a holding time of 2 h at each temperature, the remaining reactants and resulting products were analyzed by Gas chromatography (GC) using a Shimadzu GC-2014ATF with a thermal conductivity detector (TCD) and a flame-ionization detector (FID). CH_4 conversion, products (C_{2+}, CO and CO_2) selectivity, and C_{2+} yield was calculated using the following equations.

$$\text{Methane conversion}: X_{CH_4}\ (\%) = \frac{F_{CH_4,feed} - F_{CH_4}}{F_{CH_4,feed}} \times 100 \qquad (7)$$

$$C_{2+}\ \text{selectivity}: S_{C_{2+}}\ (\%) = \frac{2\left(F_{C_2H_4} + F_{C_2H_6}\right)}{2\left(F_{C_2H_4} + F_{C_2H_6}\right) + F_{CO_2} + F_{CO}} \times 100 \qquad (8)$$

$$CO\ \text{selectivity}: S_{CO}\ (\%) = \frac{F_{CO}}{2\left(F_{C_2H_4} + F_{C_2H_6}\right) + F_{CO_2} + F_{CO}} \times 100 \qquad (9)$$

$$CO_2\ \text{selectivity}: S_{CO_2}(\%) = \frac{F_{CO_2}}{2\left(F_{C_2H_4} + F_{C_2H_6}\right) + F_{CO_2} + F_{CO}} \times 100 \qquad (10)$$

$$C_{2+}\ \text{yield}: Y_{C_{2+}}\ (\%) = \frac{X_{CH_4} \times S_{C_{2+}}}{100} \qquad (11)$$

3. Results and discussion

3.1. Morphology analysis of the MnO_2 nanowires

The morphologies of MnO_2 nanostructures with different hydrothermal times were investigated using a field emission scanning electron

Fig. 1. Rig schematic diagram of OCM process.

microscope (FE-SEM), shown in Fig. 2. The morphology of MnO_2 at a hydrothermal time of 8 h (Fig. 2a) showed a mixture of rod-shaped (diameter of 18–19 nm) and sheet-shaped morphology, which can be attributed to the insufficient hydrothermal time to form nanowires [36]. Fig. 2b shows that the preparation of MnO_2 nanowires at hydrothermal time of 12 h led to a complete formation of the nanowire morphology with the smallest diameter of 14–16 nm and the longest lengths compared to other preparation times. After increasing the hydrothermal times to 17 (Fig. 2c) and 24 h (Fig. 2d), the rod-shaped morphology was observed with a larger diameter of 19–20 nm and 24–25 nm, respectively. The larger diameter and agglomeration of the nanorods could indicate the subsequent growth of MnO_2 nanowires [37]. However, the length of the nanowires was shorter at a high hydrothermal time than at a time of 12 h. This was again possibly due to long hydrothermal time can induce thermal stress within the nanowire structure leading to grain growth in the material, crack initiation and propagation which can change the structure of the wires resulting in the formation of rod-like shapes.

3.2. Structural analysis of the synthesized catalysts

Fig. 3 shows the XRD patterns of pure MnO_2 compared with NWs-8, NWs-12, NWs-17, and NWs-24. The XRD pattern of MnO_2 displays two domain phases. The major is tetragonal $MnO_2(H_2O)_{0.15}$ with I4/m space group (PDF No. 01–074-4231) diffraction peaks located at 2θ = 12.6, 17.8, 28.4, 37.5, 41.8, 49.5, 55.5, 59.7, 65.2 and 68.8°, which correspond to the (110), (200), (130), (211), (240), (141), (600), (620), (002) and (541) planes, respectively. The minor peaks are observed at 2θ = 15.1, 19.5, 21.4, 27.7 and 32.9° which can be assigned to the (111), (201), (211), (301) and (321) planes of cubic $NH_4Mn_2(SO_4)_3$ having I/Ic space group (PDF No. 01–073-3083). $NH_4Mn_2(SO_4)_3$ as impurity phase can be formulated through the (1) main reaction is $MnSO_4$ + $(NH_4)_2S_2O_8$ + $2H_2O$ → MnO_2 + $(NH_4)_2SO_4$ + $2H_2SO_4$ and (2) side reaction is $2MnSO_4$ + $(NH_4)_2SO_4$ → $(NH_4)_2Mn_2(SO_4)_3$. NWs-8, NWs-12, NWs-17, and NWs-24 demonstrated similar peaks at the diffraction angle of 2θ = 21.8, 32.1 and 37.5° which correspond to amorphous of SiO_2 (PDF No. 01–077-8669), cubic Na_2WO_4 (PDF No. 00–012-0772) and MnO_2 (PDF No. 01–074-4231), respectively. In addition, the lower intensity of the diffraction peaks of MnO_2 and Na_2WO_4 was observed because their crystal structures were partially covered by the amorphous phase of SiO_2. However, the crystal sizes of Na_2WO_4 and MnO_2 in all nanowires catalysts can be still calculated using the Scherrer equation as shown in Table 1. The calculated crystal sizes were in the range of 55–65 nm for Na_2WO_4 and 10–12 nm for MnO_2.

3.3. Acidic and basic surface sites of the synthesized catalysts

Acidity of the synthesized catalysts were measured based on the strength of chemisorbed NH_3 on the catalyst surface as shown in Fig. 4 and Table 2. Typically, the NH_3-TPD profile can be divided into three types depending on the strength of interaction between NH_3 molecule and acid site on the catalyst surface which are weak sites (<250 °C), medium sites (250–450 °C) and strong sites (>450 °C) [38]. Nevertheless, only weak sites can be observed on the surface of all synthesized catalysts. Table 2 reveals that the powdered catalyst surface had the lowest quantity of adsorbed NH_3 (6.58 μmol/g), which was significantly lower than the adsorbed NH_3 on other nanowire catalyst surfaces (440–760 μmol/g). The quantity of acid sites of all the nanowire catalysts increased in the following order: NWs-8 < NWs-12 < NWs-24 < NWs-17.

Fig. 5 shows CO_2-TPD profile of a) powdered 2%Mn-5%Na_2WO_4/ SiO_2, b) NWs-8, c) NWs-12, d) NWs-17, and e) NWs-24. The amount of CO_2 can be used as an indicator of the strength of the surface basicity. The CO_2-TPD profiles revealed three desorption peaks, indicating that CO_2 is adsorbed on the basic surface of the catalyst [39]. The weak CO_2 adsorption occurred as the first peak during low temperature range
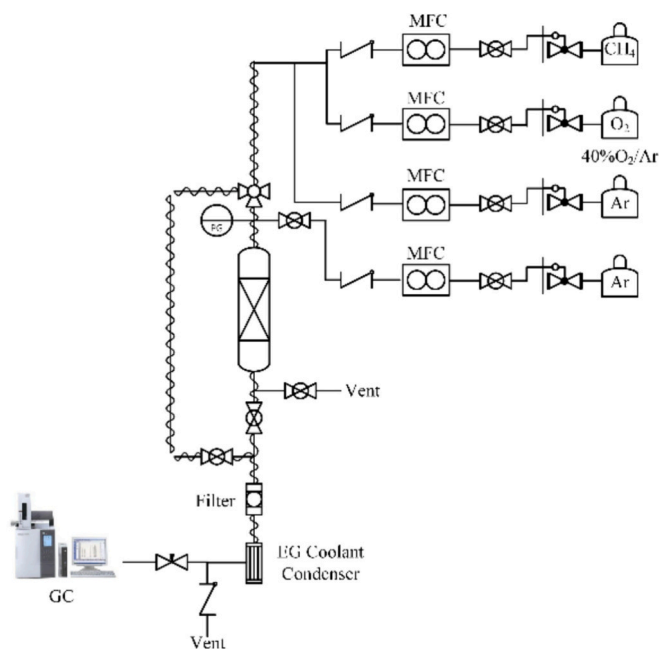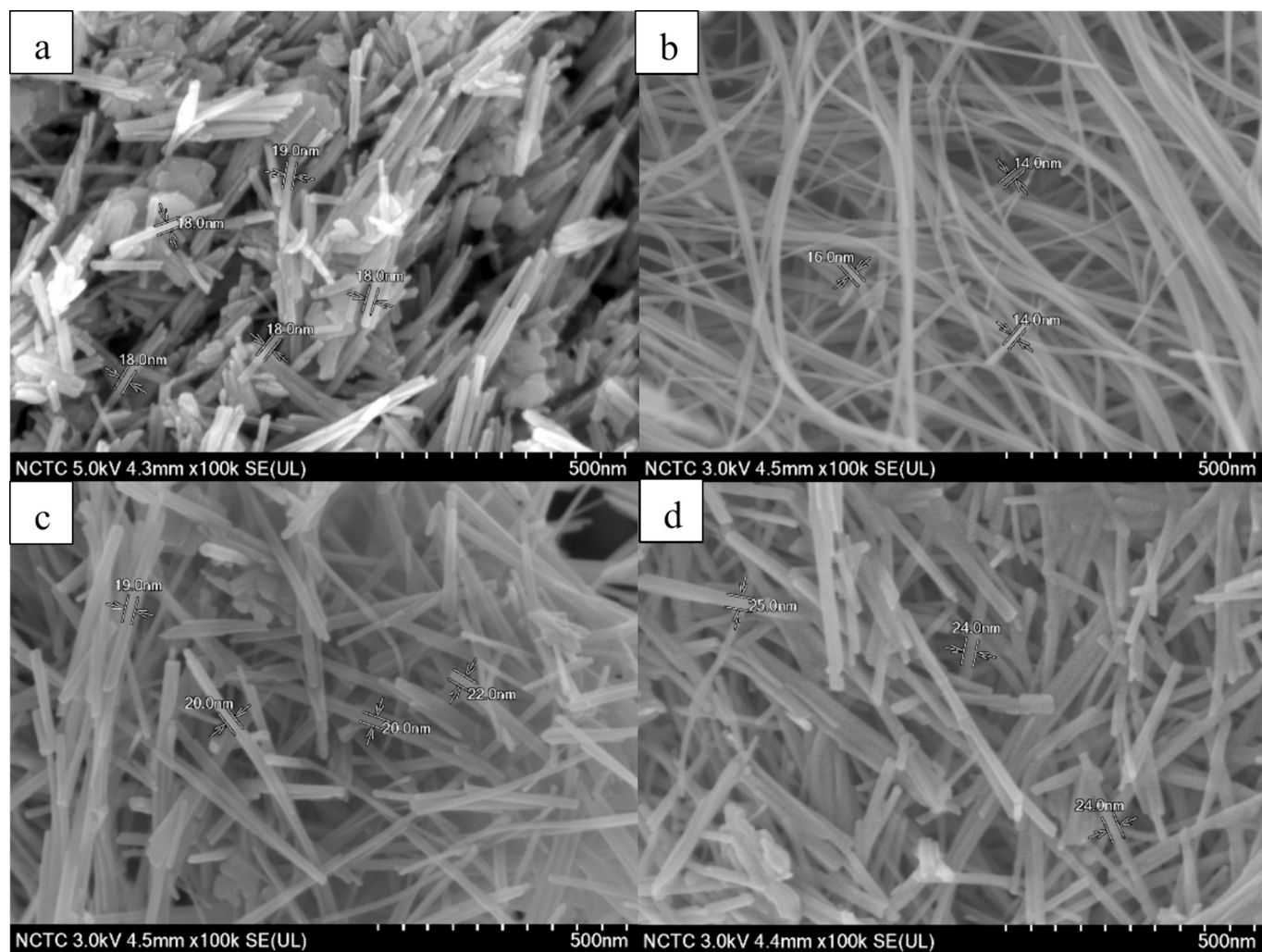
Fig. 2. FE-SEM images of MnO_2 nanostructures at different times of hydrothermal treatment; (a) 8 h, (b) 12 h, (c) 17 h and (d) 24 h without calcination.
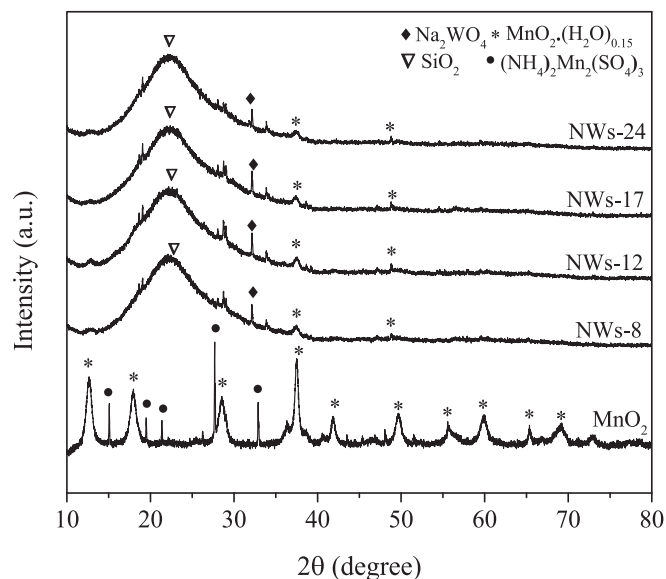

Fig. 3. XRD patterns of MnO_2-reference (no calcination) and 2%Mn-5% Na_2WO_4/SiO_2 as NWs-8, NWs-12, NWs-17, and NWs-24.

Table 1
Calculated crystal size for fresh and spent nanowire-structured 2%Mn-5% Na_2WO_4-SiO_2.

Catalyst		Crystal size (nm)			
		Na_2WO_4	MnO_2	Mn_2O_3	Mn_3O_4
NWs-8	Fresh	72.0	12.0	–	–
	Spent	33.8	42.9	72.8	41.1
NWs-12	Fresh	62.9	12.7	–	–
	Spent	54.4	41.7	69.1	–
NWs-17	Fresh	61.5	13.2	–	–
	Spent	55.8	–	72.3	–
NWs-24	Fresh	62.4	13.0	–	–
	Spent	43.2	–	81.8	–

(<250 °C), whereas the moderate and strong CO_2 adsorption occurred at temperature range of 250–500 °C and > 500 °C, respectively. Based on the data presented in Fig. 5, it can be observed that the powder 2%Mn-5%Na_2WO_4/SiO_2 catalyst exhibited negligible CO_2 desorption below 500 °C, suggesting the presence of only a small quantity of weak and moderate basic sites on its surface. In contrast, the CO_2-TPD profiles of all the nanowire-structured 2%Mn-5%Na_2WO_4/SiO_2 catalysts exhibited multiple CO_2 desorption peaks, indicating the presence of a larger number of basic sites with different degrees of strength. Table 2 shows the amounts of basic sites on the catalyst surface.
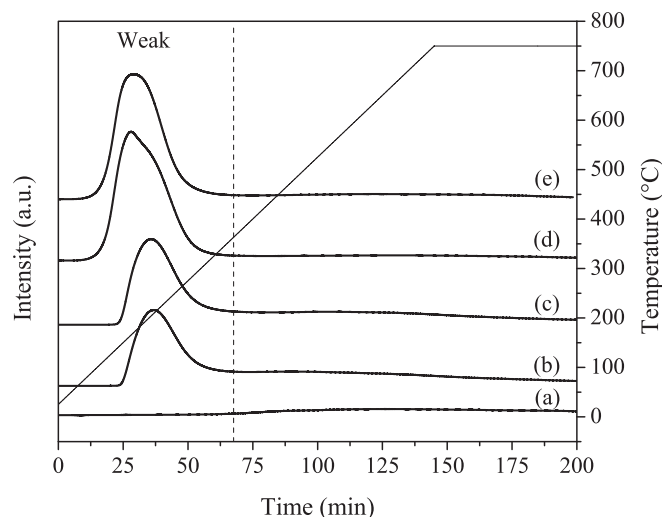
Fig. 4. NH$_3$-TPD profiles of (a) powdered 2%Mn-5%Na$_2$WO$_4$/SiO$_2$ and all the nanowires which are, (b) NWs-8, (c) NWs-12, (d) NWs-17, and (e) NWs-24.

Table 2
The amounts of acid and basic sites of the synthesized catalysts.*

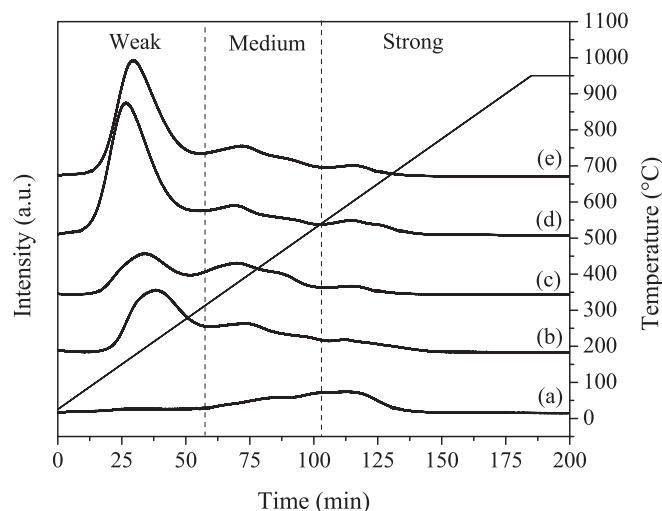| Catalyst	Powder	NWs-8	NWs-12	NWs-17	NWs-24
Acid site					
Weak	6.58	441.55	493.54	763.47	716.21
Basic site					
Weak	5.21	49.85	29.58	92.41	79.93
Medium	10.74	28.49	42.30	28.12	30.21
Strong	38.99	8.69	12.39	10.86	6.91
Total	54.94	87.02	84.28	131.39	117.05

* Unit is μmol/g

Fig. 5. CO$_2$-TPD profile of (a) powdered 2%Mn-5%Na$_2$WO$_4$/SiO$_2$ and all the nanowires which are, (b) NWs-8, (c) NWs-12, (d) NWs-17, and (e) NWs-24.

3.4. Effect of reaction temperatures

The catalytic activities of the nanowire-structured 2%Mn-5%Na$_2$WO$_4$/SiO$_2$ towards OCM were investigated and compared to the powdered catalyst. The performance of the synthesized catalysts at reaction temperatures from 650 °C to 800 °C is shown in Figs. 6 and 7. Fig. 6 shows the relationship between CH$_4$ conversion and C$_{2+}$
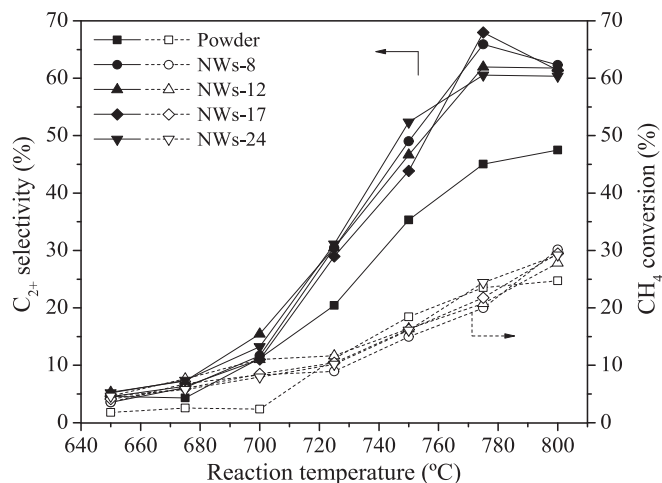

Fig. 6. Effect of reaction temperature from 650 °C to 800 °C on the activity of powdered and nanowire-structured 2%Mn-5%Na$_2$WO$_4$/SiO$_2$ catalysts with variable hydrothermal treatment times as NWs-8, NWs-12, NWs-17and NWs-24.

selectivity as a function of reaction temperature while Fig. 7 displays the distribution of products (C$_{2+}$, CO and CO$_2$) selectivity, C$_{2+}$ yield and carbon balances at various operating temperatures. The calculated carbon balances for all catalysts across all reaction temperature ranges were approximately 100%, confirming the efficiency and accuracy of the methodology and experimental procedures. The CH$_4$ conversion, C$_{2+}$ selectivity and C$_{2+}$ yield of all synthesized catalysts increased with increasing reaction temperature, indicating that the OCM process required a high temperature to activate CH$_4$. However, the C$_{2+}$ selectivity of all nanowire-structured catalysts slightly decreased after reaching 800 °C. The decrease in C$_{2+}$ selectivity and increase in CO and CO$_2$ selectivity at 800 °C were attributed to the formation of side reactions such as the C$_{2+}$ combustion and CH$_4$ steam reforming, which were more preferred at such high temperatures [40]. Furthermore, deactivation of the catalyst due to 1) coke formation on the catalyst surface, 2) melting and leaching of the active site and 3) aggregation of active metal species may contribute to the loss of C$_{2+}$ selectivity at high temperatures. At high temperature (800 °C), the structure of the catalysts can be changed by partial melting (active Na$_2$WO$_4$ species can be melted at the temperature around 700 °C [41]), leaching and aggregation of active species resulting in partial deactivation.

3.5. Effect of MnO$_2$ nanowire

When comparing the catalytic activity of nanowire-structured catalysts to powdered catalyst, it was clearly seen in Figs. 6 and 7 that all nanowire catalysts exhibited significantly higher CH$_4$ conversion, C$_{2+}$ selectivity, and C$_{2+}$ yield for all reaction temperatures (650–800 °C) than powdered catalysts. In addition, the nanowire-structured can shift the OCM operating temperature to low-temperature regions (650–700 °C). When comparing the activity of nanowire catalysts synthesized using different hydrothermal times (NWs-8, NWs-12, NWs-17, and NWs-24), it was found that NWs-12 performed the best at such reaction temperatures. This was possible due to the complete formation of nanowires with the smallest diameter, longest lengths and absence of nanowire aggregation as mentioned in the FE-SEM results, resulting in an increased surface area and more adsorbed surface oxygen [42] for NWs-12 and thus a large catalytic activity. Moreover, the acid and basic sites on the nanowire catalysts also significantly affected on the OCM catalytic performance. From CO$_2$-TPD results, NWs-12 exhibited the most amount of medium basic sites leading to the best catalytic performance due to the fact that medium basic sites on the catalyst surface are beneficial to the C$_{2+}$ production [29,30]. For the effect of acid site on
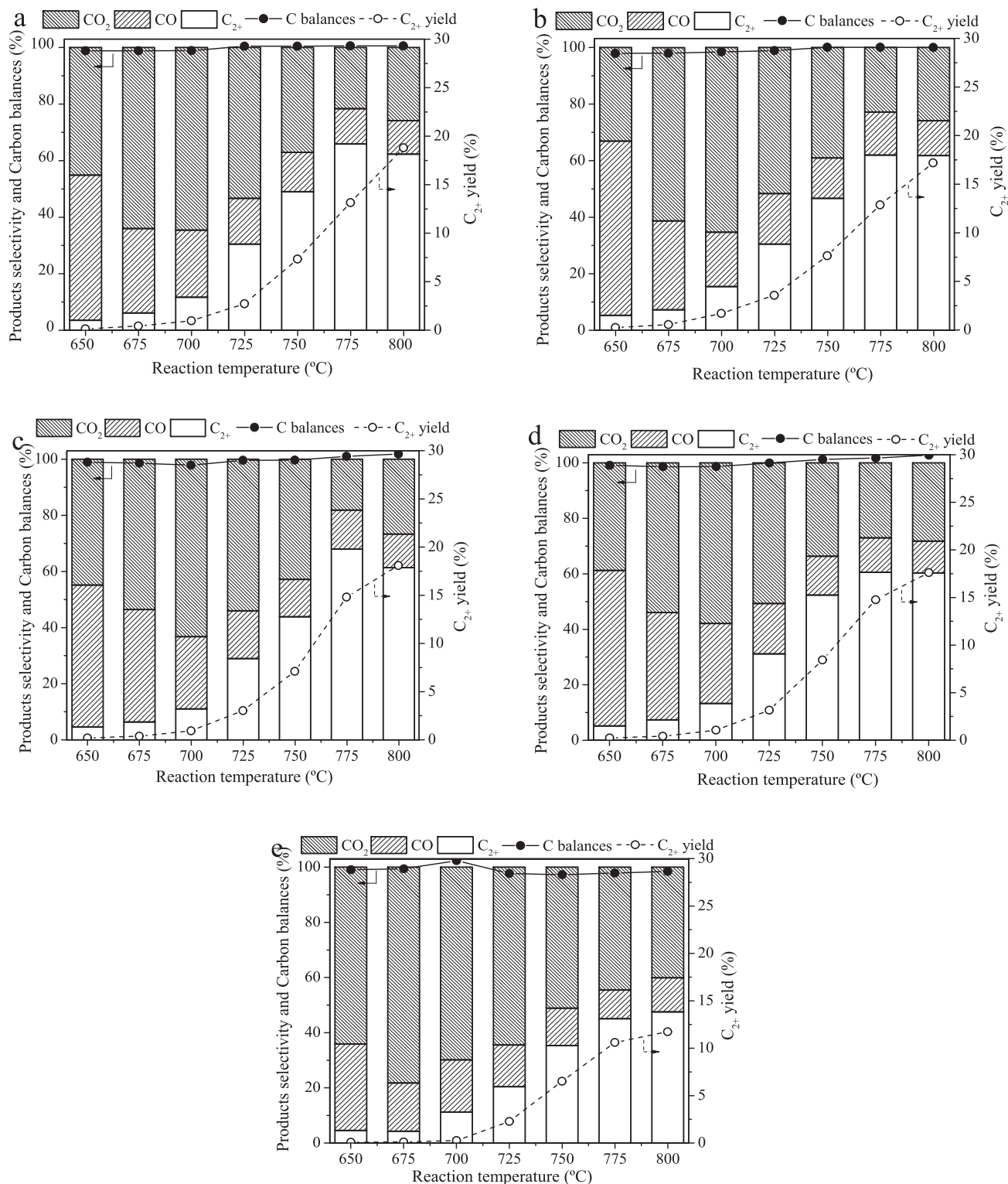
Fig. 7. Effect of reaction temperature on products selectivity, C_{2+} yield and carbon balances of nanowire-structured (a) NWs-8, (b) NWs-12, (c) NWs-17, (d) NWs-24 and (e) powdered 2%Mn-5%Na$_2$WO$_4$/SiO$_2$.

the surface, if the numbers of acid sites are too large or too small than that required, the catalyst will display poor performance in the OCM process. From our results, NWs-12 with the highest activity provided the number of weak acid site more than NWs-8 and also lower than NWs-24 and NWs-17 which was consistent with E. R. Choudhary et al. [38]. The CH$_4$ conversion, C_{2+} selectivity, and C_{2+} yield of NWs-12 at 700 °C were found to be approximately 11.0, 15.0, and 1.7%, respectively, whereas

the powdered form was only around 2.0, 11.0, and 0.3%. In other words, the nanowire-structured has the potential to improve catalytic performance at 700 °C in terms of CH$_4$ conversion, C_{2+} selectivity, and C_{2+} yield by about 5.5, 1.4, and 5.7 times, respectively, compared to the powdered form. These results indicated that the shape of the synthesized MnO$_2$ had a significant impact on the catalyst's performance, which is consistent with many previous studies [43–46]. Although nanowire

catalysts fully maintained their nanowire form at temperatures below 700 °C, they began to lose their characteristic structure at higher temperatures where the oxidative coupling of methane (OCM) is more favorable. Specifically, the advantages of the nanowire structure became less significant at these elevated temperatures. Consequently, NWs-12 was not the best catalyst at 775 °C; instead, NWs-17 performed better. This improved performance of NWs-17 could be attributed to the complete conversion of MnO_2 to Mn_2O_3, which also serves as an active site in addition to Na_2WO_4 for OCM. W. Chen and co-workers [47] discovered that manganese oxide nanowires maintained their wire-like shape even after thermal treatment at 600 °C, and then fused into particles after further increased the calcination temperature. To examine the morphology changes of the nanowire catalyst at high reaction temperatures, the $2\%Mn-5\%Na_2WO_4/SiO_2$ catalyst with the hydrothermal time of 12 h (NWs-12) was selected as a representative due to its most complete nanowire shape. Fig. 8(a) and (b) display the FE-SEM images of the NWs-12 catalyst before and after the OCM reaction at 775 °C, respectively. The results showed that the nanowire structure of the NWs-12 catalyst before the reaction still appeared the nanowire shape of MnO_2 deposited on the small particle of the amorphous SiO_2 support while that of after the reaction at 775 °C was not observed due to it was destroyed to form irregular particles deposited on the large particle of crystalline SiO_2 support at high reaction temperatures. The SEM-EDS analysis was used to analyze the presence of metal in the selected rectangular area as shown in Fig. 8(c) and (d) for the NWs-12 before and after the OCM process, respectively. In other words, the catalytic performance of the synthesized nanowire catalysts was not affected by the shape of the MnO_2 after further increasing the reaction temperature to above 700 °C. Nevertheless, all NWs catalysts still showed significantly higher activity than powdered catalyst at high reaction temperatures (700–800 °C) in which NWs-17 exhibited the best performance at 775 °C. This can be described by the phase compositions of the active

species in their structures which will be extensively explained in Section 3.6.

3.6. Effect of phase compositions

The XRD patterns of the spent catalysts (Fig. 9) proved the phase structure of the catalyst after activity study for oxidative coupling of methane at 775 °C (molar ratio of $CH_4:O_2 = 4$, WHSV = 8572 ml/h/g).
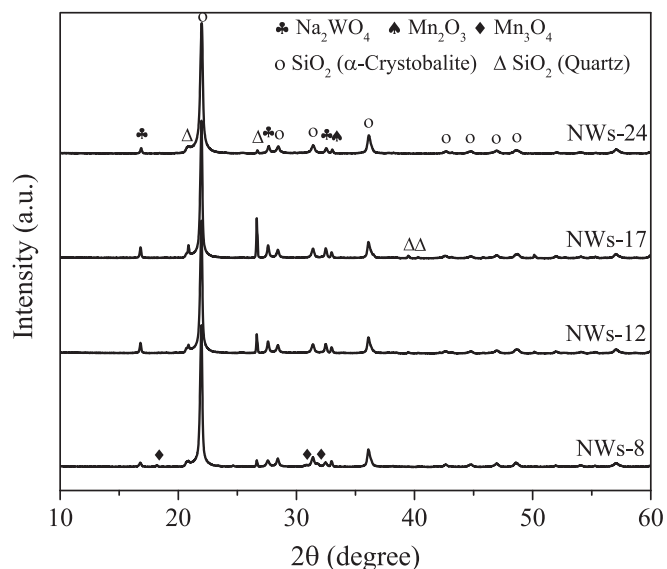
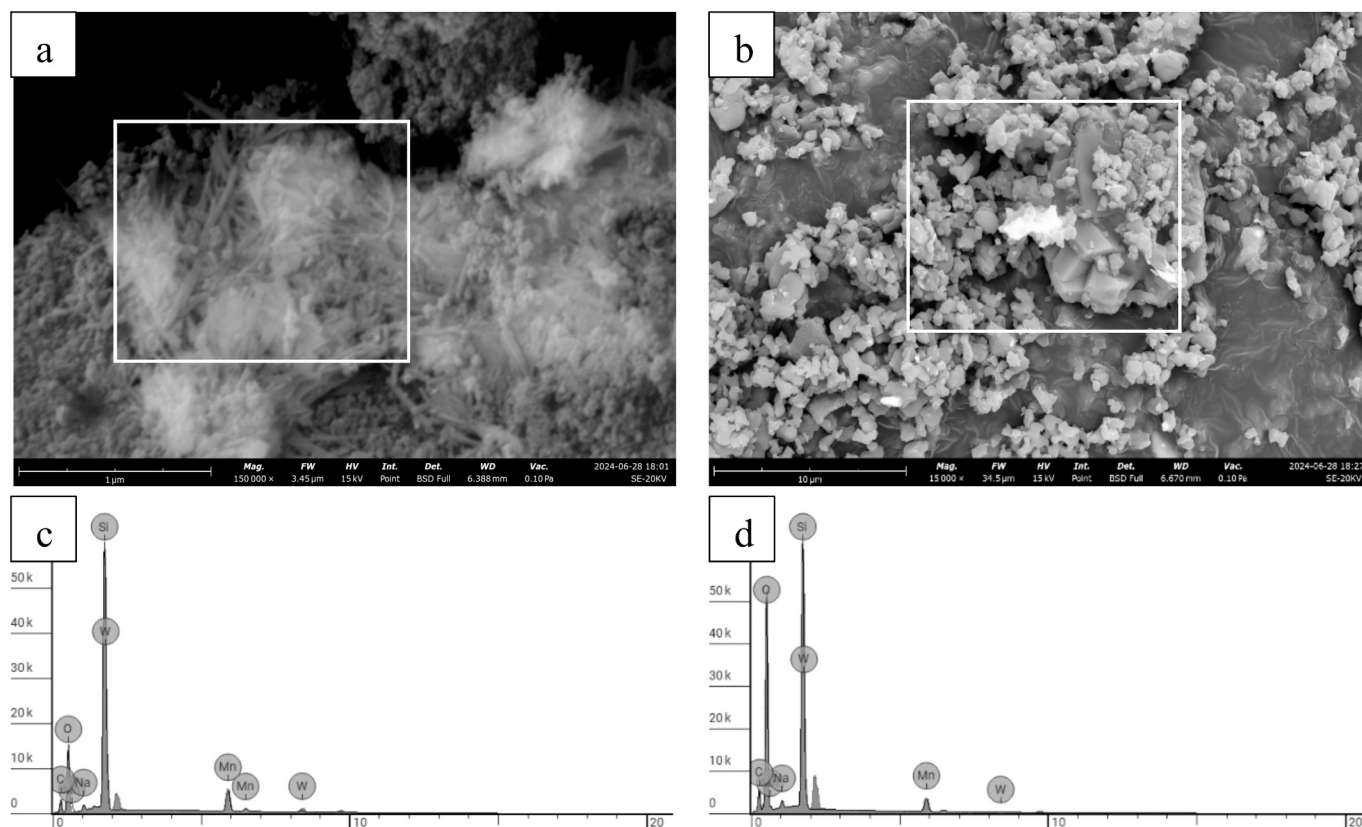**Fig. 9.** XRD patterns of spent $2\%Mn-5\%Na_2WO_4-SiO_2$ as NWs-8, NWs-12, NWs-17, and NWs-24 after OCM reaction at 775 °C.

Fig. 8. FE-SEM images of the nanowire-structured $2\%Mn-5\%Na_2WO_4/SiO_2$ catalyst with the hydrothermal time of 12 h (NWs-12) and energy dispersive X-ray spectroscopy (EDS) analysis in the selected rectangular area before [(a) and (c)] and after [(b) and (d)] the OCM reaction at 775 °C.
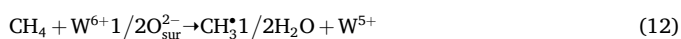
Diffraction peaks in the XRD patterns of all spent nanowire catalysts (NWs-8, NWs-12, NWs-17 and NWs-24) are assigned to cristobalite SiO$_2$, quartz SiO$_2$, Na$_2$WO$_4$ and Mn$_2$O$_3$ structure. The diffraction peaks of cristobalite SiO$_2$ were observed as the main phase at 21.9, 28.4, 31.4, 36.1, 42.6, 44.8, 47.0 and 48.5° corresponding to crystal planes of 101, 111, 102, 200, 211, 202, 113 and 212, respectively (PDF No. 01–071-6244). The presence of Quartz SiO$_2$ phase at 20.9, 26.7, 36.7 and 39.5° in agreement with PDF No. 01–085-0865. The peaks related to Na$_2$WO$_4$ appeared at 16.8, 27.6 and 32.5° corresponding to 111, 220 and 311 planes, respectively (PDF No. 01–084-6510). The peaks observed at 33.0° corresponded to the Mn$_2$O$_3$ structure (PDF No. 01–073-1826). However, the additional peaks at 18.1, 31.1 and 32.5° were found for NWs-8 which are related to 101, 200 and 103 planes of Mn$_3$O$_4$, respectively (PDF No. 01–075-1560). In addition, MnO$_2$ phase was also found in spent NWs-8 and NWs-12. Although the MnO$_2$ peak cannot be noticed since it appears at the same position as cristobalite SiO$_2$ (28.4°), XRD fitting can confirm its existence. Table 1 shows the crystal size analysis of all compounds in spent catalysts using the Scherrer equation.

Compared to the fresh catalyst, the amorphous silica support in all synthesized catalysts was crystallized to α-cristobalite at a reaction temperature of 775 °C. The inclusion of Na ions in the catalyst induced a phase transformation of SiO$_2$ from its amorphous to a cristobalite structure at low temperature. On the other hand, the transformation of pure SiO$_2$ was observed at higher temperature approximately 1500 °C [48–50]. The phase transition from amorphous to crystalline SiO$_2$ appears to be a necessary component for an effective catalyst to be used in OCM [48]. Furthermore, the MnO$_2$ phase was converted to Mn$_2$O$_3$ for NWs-12, NWs-17, and NWs-24, as well as a combination of Mn$_2$O$_3$ and Mn$_3$O$_4$ for NWs-8, with some MnO$_2$ phase remaining in NWs-8 and NWs-12. However, after activity testing at 775 °C, the structure of Na$_2$WO$_4$ in all spent catalysts remained unchanged when compared to the fresh catalyst. The characteristic peak of Na$_2$WO$_4$ still appeared in the absence of the other phase of W species for all catalysts. Therefore, the catalytic activity may depend on the different Mn species in the catalyst as the main factor.

The OCM catalytic performance results in Figs. 6 and 7 shows that NWs-17 had the highest catalytic activity at reaction temperature of 775 °C, with CH$_4$ conversion, C$_{2+}$ selectivity, and C$_{2+}$ yield of 21.8, 68.0 and 14.8%, respectively. As mentioned in the previous part, the catalytic activity of the synthesized nanowire catalysts at the reaction temperatures higher than 700 °C was unaffected by the shape of the MnO$_2$ due to MnO$_2$ morphology in all nanowire catalysts can be destroyed under high temperatures. Therefore, the activity of all nanowire catalysts can be described by phase compositions of active species in their structures.

The OCM reaction mechanism consists of heterogeneous (surface catalysts) and homogeneous (gas phase) reactions as shown in Eqs. (12)–(16). The OCM mechanism over the Mn-Na$_2$WO$_4$/SiO$_2$ catalyst involves two metal sites, consisting of W$^{6+/5+}$ and Mn$^{3+/2+}$. At the catalyst surface, the W$^{6+/5+}$ sites help to activate methane, while the Mn$^{3+/2+}$ sites help to activate oxygen. The CH$_4$ is activated by O$_{sur}^{\bullet}$ to generate CH$_3^{\bullet}$ at the W$^{6+/5+}$ site and then electron transferred from the W$^{6+/5+}$ site to the Mn$^{3+/2+}$ site, which is responsible for the activation of oxygen gas to form the surface oxygen (O$_{sur}^{2-}$) as the active oxygen species for CH$_4$ activation. After that, the coupling reaction between CH$_3^{\bullet}$ occurred in the gas phase to form ethane (C$_2$H$_6$) which was further dehydrogenated to produce ethylene (C$_2$H$_4$) and hydrogen (H$_2$) [51].

Surface reaction

$$CH_4 + W^{6+} 1/2O_{sur}^{2-} \rightarrow CH_3^{\bullet} 1/2H_2O + W^{5+} \tag{12}$$

$$W^{5+} + Mn^{3+} \rightarrow W^{6+} + Mn^{2+} \tag{13}$$

$$1/4O_2 + Mn^{2+} \rightarrow 1/2O_{sur}^{2-} + Mn^{3+} \tag{14}$$

Gas-phase coupling reaction

$$CH_3^{\bullet} \rightarrow 1/2C_2H_6 \tag{15}$$

Gas-phase dehydrogenation reaction

$$C_2H_6 \rightarrow C_2H_4 + H_2 \tag{16}$$

According to the OCM mechanisms, Na$_2$WO$_4$ (W^{6+}) and Mn$_2$O$_3$ (Mn^{3+}) species can be considered active sites for methane and oxygen activation, respectively. While MnO$_2$ (Mn^{4+}) may be excessively oxidizing, resulting in oxidized products such as CO and CO$_2$. Moreover, it is also possible that MnO$_2$ does not have the appropriate geometry for critical interactions with tungsten [52]. Therefore, a catalyst containing MnO$_2$ would exhibit lower catalytic activity for OCM compared to a catalyst consisting solely of Mn$_2$O$_3$. According to the XRD results of the spent catalysts in Fig. 9, the presence of MnO$_2$ species in NWs-8 and NWs-12 caused them to be less active than NWs-17 at the reaction temperature of 775 °C. Nevertheless, even though the MnO$_2$ phase did not appear in NWs-24, it exhibited lower activity than NWs-17 due to the larger crystal size of Mn$_2$O$_3$ (Table 1), resulting in a smaller active surface to activate CH$_4$ compared to NWs-17. Furthermore, the reduced XRD peak intensity of Na2WO4 was also observed for NWs-8 and NWs-24, suggesting partial melting and leaching of active Na2WO4 species at elevated temperatures. These findings help elucidate the catalytic activity observed across all catalysts, showing decreased C2+ selectivity in the following sequence: NWs-17 > NWs-8 > NWs-12 > NWs-24.

3.7. Stability test of the best catalyst (NWs-17) for OCM reaction at 775 °C

Time-on-stream testing of the catalyst is also critical for OCM reaction at high temperatures due to 1) coke creation on the catalyst surface, 2) melting and leaching of the active site, and 3) aggregation of active metal species, which causes the catalyst to deactivate rapidly. In this study, catalytic performance was tested on stream at 775 °C for 300 min. Fig. 10 shows the CH$_4$ conversion, C$_{2+}$ yield, and C$_{2+}$ selectivity of the best catalyst (NWs-17) as a function of reaction time. It can be seen that the NWs-17 catalyst enhanced its activity in terms of CH$_4$ conversion, C$_{2+}$ yield and C$_{2+}$ selectivity within the first 50 min. After this activation period, a stable CH$_4$ conversion, C$_{2+}$ yield and C$_{2+}$ selectivity was observed throughout the entire time on stream with no obvious deactivation. In other words, the NWs-17 catalyst displayed high activity and thermal stability at 775 °C for 300 min on stream.
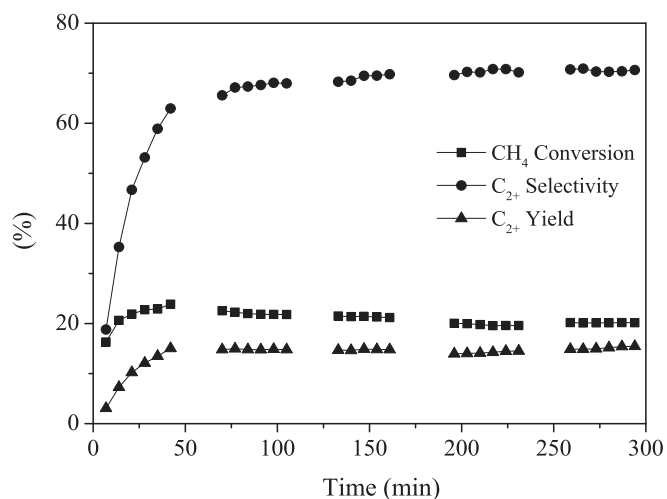

Fig. 10. CH$_4$ conversion, C$_{2+}$ yield and C$_{2+}$ selectivity of NWs-17 catalyst as a function of time-on-stream for OCM reaction at 775 °C (molar ratio of CH$_4$:O$_2$ = 4, WHSV = 8572 ml/h/g).

4. Conclusions

Nanowire-structured 2%Mn-5%Na$_2$WO$_4$/SiO$_2$ catalysts were successfully synthesized by hydrothermal method. NWs-12 provided the smallest diameter with the longest lengths. This structure contributed to the higher CH$_4$ conversion and C$_{2+}$ selectivity as well as lower operating temperature due to the reduced activation energy for C$_{2+}$ production reaction. Furthermore, the acid and basic sites on the nanowire catalyst significantly affected the OCM catalytic performance. NWs-12 catalyst exhibited the highest quantity of medium basic sites and a moderate amount of acid sites on its surface, resulting in the highest activity for OCM at the reaction temperature of 700 °C. Although nanowire catalysts fully maintained their nanowire form at temperatures below 700 °C, they began to lose their characteristic structure at higher temperatures where the oxidative coupling of methane (OCM) is more favorable. Specifically, the advantages of the nanowire structure became less significant at these elevated temperatures. Consequently, NWs-12 was not the best catalyst at 775 °C; instead, NWs-17 performed better. This improved performance of NWs-17 could be attributed to the complete conversion of MnO$_2$ to Mn$_2$O$_3$, which also serves as an active site in addition to Na$_2$WO$_4$. Na$_2$WO$_4$ and Mn$_2$O$_3$ exhibit synergy as the active sites for the OCM reaction. The NWs-17 catalyst displayed high activity and thermal stability at 775 °C for 300 min on stream.

CRediT authorship contribution statement

I. Sereewatthanawut: Writing – original draft, Resources, Project administration. **V. Tongnan:** Writing – original draft, Validation, Methodology, Investigation, Formal analysis. **R. Ampairojanawong:** Validation, Formal analysis, Data curation. **A. Makdee:** Visualization, Investigation, Formal analysis, Data curation, Conceptualization. **N. Swadchaipong:** Validation, Project administration. **P. Maneesard:** Software, Project administration. **K. Li:** Writing – review & editing, Supervision. **U.W. Hartley:** Writing – review & editing, Supervision, Resources, Project administration, Funding acquisition, Conceptualization.

Declaration of competing interest

The authors declare the following financial interests/personal relationships which may be considered as potential competing interests:

Unalome W. Hartley reports financial support was provided by King Mongkut's University of Technology North Bangkok. If there are other authors, they declare that they have no known competing financial interests or personal relationships that could have appeared to influence the work reported in this paper.

Data availability

Data will be made available on request.

Acknowledgments

References

[1] O. Badr, S.D. Probert, P.W. O'Callaghan, Atmospheric methane: its contribution to global warming, Appl. Energy 40 (1991) 273–313, https://doi.org/10.1016/0306-2619(91)90021-O.

[2] M. Evans, V. Roshchanka, Russian policy on methane emissions in the oil and gas sector: a case study in opportunities and challenges in reducing short-lived forcers, Atmos. Environ. 92 (2014) 199–206, https://doi.org/10.1016/j.atmosenv.2014.04.026.

[3] J. Cooper, L. Stamford, A. Azapagic, Shale gas: a review of the economic, environmental, and social sustainability, Energy Technol. 4 (2016) 772–792, https://doi.org/10.1002/ente.201500464.

[4] C. Aktemur, An overview of natural gas as an energy source for various purposes, Int. J. Eng. Technol. IJET 3 (2017) 91–104, https://doi.org/10.19072/ijet.300750.

[5] M.H. Almatarneh, A. Alnajajrah, M. Altarawneh, Y. Zhao, M.A. Halim, Computational mechanistic study of the unimolecular dissociation of ethyl hydroperoxide and its bimolecular reactions with atmospheric species, Sci. Rep. 10 (2020) 1–22, https://doi.org/10.1038/s41598-020-71881-3.

[6] L. Chen, Z. Qi, S. Zhang, J. Su, G.A. Somorjai, Catalytic Hydrogen Production from Methane, 2020.

[7] A. Iulianelli, S. Liguori, J. Wilcox, A. Basile, Advances on methane steam reforming to produce hydrogen through membrane reactors technology: a review, Catal. Rev. Sci. Eng. 58 (2016) 1–35, https://doi.org/10.1080/01614940.2015.1099882.

[8] P. Summa, B. Samojeden, M. Motak, Dry and steam reforming of methane. Comparison and analysis of recently investigated catalytic materials. A short review, Pol. J. Chem. Technol. 21 (2019) 31–37, https://doi.org/10.2478/pjct-2019-0017.

[9] S. Arora, R. Prasad, An overview on dry reforming of methane: strategies to reduce carbonaceous deactivation of catalysts, RSC Adv. 6 (2016) 108668–108688, https://doi.org/10.1039/c6ra20450c.

[10] J.M. Lavoie, Review on dry reforming of methane, a potentially more environmentally-friendly approach to the increasing natural gas exploitation, Front. Chem. 2 (2014) 1–17, https://doi.org/10.3389/fchem.2014.00081.

[11] C. Alvarez-Galvan, M. Melian, L. Ruiz-Matas, J.L. Eslava, R.M. Navarro, M. Ahmadi, B.R. Cuenya, J.L.G. Fierro, Partial oxidation of methane to syngas over nickel-based catalysts: influence of support type, addition of rhodium, and preparation method, Front. Chem. 7 (2019) 1–16, https://doi.org/10.3389/fchem.2019.00104.

[12] A.H. Elbadawi, L. Ge, Z. Li, S. Liu, S. Wang, Z. Zhu, Catalytic partial oxidation of methane to syngas: review of perovskite catalysts and membrane reactors, Catal. Rev. Sci. Eng. 63 (2021) 1–67, https://doi.org/10.1080/01614940.2020.1743420.

[13] L. Li, N.H. Md Dostagir, A. Shrotri, A. Fukuoka, H. Kobayashi, Partial oxidation of methane to syngas via Formate intermediate found for a ruthenium-rhenium bimetallic catalyst, ACS Catal. 11 (2021) 3782–3789, https://doi.org/10.1021/acscatal.0c05491.

[14] R. Kundu, V. Ramasubramanian, S.T. Neeli, H. Ramsurn, Catalytic pyrolysis of methane to hydrogen over carbon (from cellulose biochar) encapsulated Iron nanoparticles, Energy Fuel 35 (2021) 13523–13533, https://doi.org/10.1021/acs.energyfuels.1c01620.

[15] N. Sánchez-Bastardo, R. Schlögl, H. Ruland, Methane pyrolysis for zero-emission hydrogen production: a potential bridge technology from fossil fuels to a renewable and sustainable hydrogen economy, Ind. Eng. Chem. Res. 60 (2021) 11855–11881, https://doi.org/10.1021/acs.iecr.1c01679.

[16] V.I. Lomonosov, M.Y. Sinev, Oxidative coupling of methane: mechanism and kinetics, Kinet. Catal. 57 (2016) 647–676, https://doi.org/10.1134/S0023158416050128.

[17] I.E.W. Daniyal Kiani, Sagar Sourav, Jonas Baltrusaitis, Oxidative coupling of methane (OCM) by SiO$_2$-supported tungsten.pdf, ACS Catal. (2019) 5912–5928.

[18] P. Wang, G. Zhao, Y. Liu, Y. Lu, TiO$_2$-doped Mn$_2$O$_3$-Na$_2$WO$_4$/SiO$_2$ catalyst for oxidative coupling of methane: solution combustion synthesis and MnTiO$_3$-dependent low-temperature activity improvement, Appl. Catal. A Gen. 544 (2017) 77–83, https://doi.org/10.1016/j.apcata.2017.07.012.

[19] F. Papa, P. Luminita, P. Osiceanu, R. Birjega, M. Akane, I. Balint, Acid-base properties of the active sites responsible for C$_{2+}$ and CO$_2$ formation over MO-Sm$_2$O$_3$ (M = Zn, Mg, Ca and Sr) mixed oxides in OCM reaction, J. Mol. Catal. A Chem. 346 (2011) 46–54, https://doi.org/10.1016/j.molcata.2011.06.008.

[20] L. Luo, R. You, Y. Liu, J. Yang, Y. Zhu, W. Wen, Y. Pan, F. Qi, W. Huang, Gas-phase reaction network of Li/MgO-catalyzed oxidative coupling of methane and oxidative dehydrogenation of ethane, ACS Catal. 9 (2019) 2514–2520, https://doi.org/10.1021/acscatal.8b04728.

[21] K. Qian, R. You, Y. Guan, W. Wen, Y. Tian, Y. Pan, W. Huang, Single-site catalysis of Li-MgO catalysts for oxidative coupling of methane reaction, ACS Catal. 10 (2020) 15142–15148, https://doi.org/10.1021/acscatal.0c03896.

[22] V.H. Rane, S.T. Chaudhari, V.R. Choudhary, Oxidative coupling of methane over La-promoted CaO catalysts: influence of precursors and catalyst preparation method, J. Nat. Gas Chem. 19 (2010) 25–30, https://doi.org/10.1016/S1003-9953(09)60023-2.

[23] L. Mleczko, U. Pannek, M. Rothaemel, M. Baerns, Oxidative coupling of methane over a La$_2$O$_3$/CaO catalyst. Optimization of reaction conditions in a bubbling fluidized-bed reactor, Can. J. Chem. Eng. 74 (1996) 279–287, https://doi.org/10.1002/cjce.5450740213.

[24] B.M. Sollier, L.E. Gómez, A.V. Boix, E.E. Miró, Oxidative coupling of methane on Sr/La$_2$O$_3$ catalysts: improving the catalytic performance using cordierite monoliths and ceramic foams as structured substrates, Appl. Catal. A Gen. 532 (2017) 65–76, https://doi.org/10.1016/j.apcata.2016.12.018.

[25] Z. Fakhroueian, F. Farzaneh, N. Afrookhteh, Oxidative coupling of methane catalyzed by Li, Na and mg doped BaSrTiO$_3$, Fuel 87 (2008) 2512–2516, https://doi.org/10.1016/j.fuel.2008.02.010.

[26] B. Huang, N.S. Hayek, G. Sun, S. Mottaghi-Tabar, D.S.A. Simakov, O.M. Gazit, Correlating properties of the Mn$_2$O$_3$-Na$_2$WO$_4$/SiO$_2$ catalyst with statistically estimated parameters for the oxidative coupling of methane, Energy Fuel 35 (2021) 9589–9598, https://doi.org/10.1021/acs.energyfuels.1c00481.

[27] W. Riedel, L. Thum, J. Möser, V. Fleischer, U. Simon, K. Siemensmeyer, A. Schnegg, R. Schomäcker, T. Risse, K.P. Dinse, Magnetic properties of reduced and Reoxidized Mn-Na$_2$WO$_4$/SiO$_2$: a catalyst for oxidative coupling of methane (OCM), J. Phys. Chem. C 122 (2018) 22605–22614, https://doi.org/10.1021/acs.jpcc.8b07386.

[28] P. Wang, X. Zhang, G. Zhao, Y. Liu, Y. Lu, Oxidative coupling of methane: MO$_x$-modified (M = Ti, Mg, Ga, Zr) Mn$_2$O$_3$-Na$_2$WO$_4$/SiO$_2$ catalysts and effect of MO$_x$ modification, Cuihua Xuebao/Chinese, J. Catal. 39 (2018) 1395–1402, https://doi.org/10.1016/S1872-2067(18)63076-1.

[29] Y.H. Hou, W.C. Han, W.S. Xia, H.L. Wan, Structure sensitivity of La$_2$O$_2$CO$_3$ catalysts in the oxidative coupling of methane, ACS Catal. 5 (2015) 1663–1674, https://doi.org/10.1021/cs501733r.

[30] T. Jiang, J. Song, M. Huo, N.T. Yang, J. Liu, J. Zhang, Y. Sun, Y. Zhu, La$_2$O$_3$ catalysts with diverse spatial dimensionality for oxidative coupling of methane to produce ethylene and ethane, RSC Adv. 6 (2016) 34872–34876, https://doi.org/10.1039/c6ra01805j.

[31] Y. Jianjun Song, R. Sun, S. Ba, Y. Huang, J. Zhao, Y. Zhang, Y. Zhua Suna, Monodisperse Sr-La$_2$O$_3$ hybrid nanofibers for oxidative coupling of methane to synthesize C$_2$ hydrocarbons, Nanoscale 7 (2015) 2260, https://doi.org/10.1039/b000000x.

[32] D. Noon, A. Seubsai, S. Senkan, Oxidative coupling of methane by nanofiber catalysts, ChemCatChem 5 (2013) 146–149, https://doi.org/10.1002/cctc.201200408.

[33] D. Noon, B. Zohour, S. Senkan, Oxidative coupling of methane with La$_2$O$_3$-CeO$_2$ nanofiber fabrics: a reaction engineering study, J. Nat. Gas Sci. Eng. 18 (2014) 406–411, https://doi.org/10.1016/j.jngse.2014.04.004.

[34] C. Karakaya, H. Zhu, B. Zohour, S. Senkan, R.J. Kee, Detailed reaction mechanisms for the oxidative coupling of methane over La$_2$O$_3$/CeO$_2$ nanofiber fabric catalysts, ChemCatChem 9 (2017) 4538–4551, https://doi.org/10.1002/cctc.201701172.

[35] R.T. Yunarti, M. Lee, Y.J. Hwang, J.W. Choi, D.J. Suh, J. Lee, I.W. Kim, J.M. Ha, Transition metal-doped TiO$_2$ nanowire catalysts for the oxidative coupling of methane, Catal. Commun. 50 (2014) 54–58, https://doi.org/10.1016/j.catcom.2014.02.026.

[36] Y. Zhao, A technology of preparing MnO$_2$ nanowire from the low grade manganese ore, MOJ Appl. Bionics Biomech. 3 (2019) 27–32, https://doi.org/10.15406/mojabb.2019.03.00096.

[37] N. Wang, H. Pang, H. Peng, G. Li, X. Chen, Hydrothermal synthesis and electrochemical properties of MnO$_2$ nanostructures, Cryst. Res. Technol. 44 (2009) 1230–1234, https://doi.org/10.1002/crat.200800619.

[38] V.R. Choudhary, V.H. Rane, S.T. Chaudhari, Surface properties of rare earth promoted MgO catalysts and their catalytic activity/selectivity in oxidative coupling of methane, Appl. Catal. A Gen. 158 (1997) 121–136, https://doi.org/10.1016/S0926-860X(96)00376-6.

[39] J. Xu, L. Peng, X. Fang, Z. Fu, W. Liu, X. Xu, H. Peng, R. Zheng, X. Wang, Developing reactive catalysts for low temperature oxidative coupling of methane: on the factors deciding the reaction performance of Ln$_2$Ce$_2$O$_7$ with different rare earth a sites, Appl. Catal. A Gen. 552 (2018) 117–128, https://doi.org/10.1016/j.apcata.2018.01.004.

[40] M. Thanasiriruk, P. Saychoo, C. Khajonvittayakul, V. Tongnan, U.W. Hartley, N. Laosiripojana, Optimizing operating conditions for oxidative coupling methane (OCM) in the presence of NaCl-MnO$_x$/SiO$_2$, Appl. Sci. Eng. Prog. 14 (2021) 477–488, https://doi.org/10.14416/j.asep.2020.10.001.

[41] E.I. Vovk, D. Wang, Z. Qiu, Y. Liu, M. He, X. Zhou, C. Guan, N. Yu, Y. Lu, J. Lang, Y. Yang, In situ structure study of a TiO$_2$ doped MnO$_x$-Na$_2$WO$_4$/SiO$_2$ catalyst under Na$_2$WO$_4$ melting conditions, Top. Catal. (2024), https://doi.org/10.1007/s11244-024-01946-4.

[42] P. Huang, Y. Zhao, J. Zhang, Y. Zhu, Y. Sun, Exploiting shape effects of La$_2$O$_3$ nanocatalysts for oxidative coupling of methane reaction, Nanoscale 5 (2013) 10844–10848, https://doi.org/10.1039/c3nr03617k.

[43] J. Li, Z. Qu, Y. Qin, H. Wang, Effect of MnO$_2$ Morphology on the Catalytic Oxidation of Toluene over ag/MnO$_2$ Catalysts, Elsevier B.V, 2016, https://doi.org/10.1016/j.apsusc.2016.05.114.

[44] B. He, G. Cheng, S. Zhao, X. Zeng, Y. Li, R. Yang, M. Sun, L. Yu, Controlled synthesis of tunnel-structured MnO$_2$ through hydrothermal transformation of δ-MnO$_2$ and their catalytic combustion of dimethyl ether, J. Solid State Chem. 269 (2019) 305–311, https://doi.org/10.1016/j.jssc.2018.09.005.

[45] T. Wang, S. Chen, H. Wang, Z. Liu, Z. Wu, In-plasma catalytic degradation of toluene over different MnO$_2$ polymorphs and study of reaction mechanism, Cuihua Xuebao/Chinese, J. Catal. 38 (2017) 793–803, https://doi.org/10.1016/S1872-2067(17)62808-0.

[46] E. Saputra, S. Muhammad, H. Sun, H.M. Ang, M.O. Tadé, S. Wang, Different crystallographic one-dimensional MnO$_=$ nanomaterials and their superior performance in catalytic phenol degradation, Environ. Sci. Technol. 47 (2013) 5882–5887, https://doi.org/10.1021/es400878c.

[47] W. Chen, N. Wang, L. Liu, Y. Cui, X. Cao, Q. Chen, L. Guo, Facile synthesis of manganite nanowires: phase transitions and their electrocatalysis performance, Nanotechnology 20 (2009), https://doi.org/10.1088/0957-4484/20/44/445601.

[48] U. Simon, O. Görke, A. Berthold, S. Arndt, R. Schomäcker, H. Schubert, Fluidized bed processing of sodium tungsten manganese catalysts for the oxidative coupling of methane, Chem. Eng. J. 168 (2011) 1352–1359, https://doi.org/10.1016/j.cej.2011.02.013.

[49] S. Hou, Y. Cao, W. Xiong, H. Liu, Y. Kou, Site requirements for the oxidative coupling of methane on SiO$_2$-supported Mn catalysts, Ind. Eng. Chem. Res. 45 (2006) 7077–7083, https://doi.org/10.1021/ie060269c.

[50] A. Palermo, J.P.H. Vazquez, A.F. Lee, M.S. Tikhov, R.M. Lambert, Critical influence of the amorphous silica-to-cristobalite phase transition on the performance of Mn/Na$_2$WO$_4$/SiO$_2$ catalysts for the oxidative coupling of methane, J. Catal. 177 (1998) 259–266, https://doi.org/10.1006/jcat.1998.2109.

[51] S.B. Li, Oxidative coupling of methane over W-Mn/SiO$_2$ catalyst, Chin. J. Chem. 19 (2001) 16–21, https://doi.org/10.1002/cjoc.20010190104.

[52] T.W. Elkins, H.E. Hagelin-Weaver, Characterization of Mn-Na$_2$WO$_4$/SiO$_2$ and Mn-Na$_2$WO$_4$/MgO catalysts for the oxidative coupling of methane, Appl. Catal. A Gen. 497 (2015) 96–106, https://doi.org/10.1016/j.apcata.2015.02.040.